Materials Science and Engineering B 264 (2021) 114971

Contents lists available at ScienceDirect

Materials Science & Engineering B

journal homepage: www.elsevier.com/locate/mseb

Structural, paramagnetic centres and luminescence investigations of the UV radiation-emitting $BaZrO_3:Gd^{3+}$ perovskite ceramic prepared via sol-gel route

Vijay Singh [a,*], S. Watanabe [b], T.K. Gundu Rao [b], G. Lakshminarayana [c]

[a] Department of Chemical Engineering, Konkuk University, Seoul 05029, Republic of Korea
[b] Institute of Physics, University of Sao Paulo, SP 05508-090, Brazil
[c] Intelligent Construction Automation Center, Kyungpook National University, 80, Daehak-ro, Buk-gu, Daegu 41566, Republic of Korea

ARTICLE INFO

Keywords:
Sol-gel
Perovskite
Ceramic
EPR
Gd^{3+} ions
$BaZrO_3$
Defect centers

ABSTRACT

Perovskite-type ceramic materials have been widely studied due to their potential use in such applications as electrical, thermal, optical, and immobilizing host materials in nuclear waste. In this work, Gd^{3+}-doped $BaZrO_3$ perovskite samples were prepared by sol-gel method and characterized by scanning electron microscopy (SEM), X-ray diffraction (XRD), electron paramagnetic resonance (EPR) spectroscopy, and photoluminescence (PL) analysis. Our XRD analysis confirmed the formation of the sol-gel products, and the SEM data implicated the prepared porous compound as the cause of the gases that evolved during the preparation. Upon excitation at 275 nm, the ceramic material displayed UVB emission at 315 nm ($^6P_{7/2} \rightarrow {}^8S_{7/2}$). The EPR technique was used to study the undoped and gadolinium-doped perovskite $BaZrO_3$ ceramics. The lines in the undoped system were caused by two defect centers. Center I displayed an isotropic line with a *g*-factor of 1.973 and a linewidth of 48 Gauss, and the center was assigned to an F^+ center. Center II exhibited an axially symmetric *g*-tensor with principal values $g_{||} = 1.895$ and $g_{\perp} = 1.978$. This center was identified as the Zr^{3+} ion. The single dominant EPR line with an effective *g*-value of 1.976 that was observed in the Gd-doped system was attributed to the Gd^{3+} ion experiencing a weak cubic symmetry crystal field.

1. Introduction

In recent years, perovskite-type ceramic has attracted much attention due to its highly stable structure, and various applied applications [1–5]. The general formula for perovskite oxides is ABO_3, where A is a rare earth (RE) or an alkali-earth element and B a transition metal. The perovskite oxides are gaining significant attention from researchers [6–10]. Based on the different doping levels of A and B, the properties of the perovskite ABO_3 oxides can be changed, and these compounds have been used for many technological applications [10–13]. Perovskite oxide materials have gained much attention based on their interesting properties in such areas as optics, superconductivity, ferroelectricity, and magnetism [13–16]. Due to comparatively high lattice oxygen mobility, these perovskite-type mixed oxides have been used in various applications in solid oxide fuel cells (SOFCs), steam electrolytes, oxygen sensors, catalysts, solid-state proton conductors, luminescent host, and nuclear waste forms for fission products [17–23].

Among the various perovskite forms, the barium zirconate ($BaZrO_3$) host is a well-known refractory material with a very high melting point (2600 °C). Along with the essential features of a very high melting point, small thermal expansion coefficient, high chemical stability, and the highest bulk protonic conductivity, doped $BaZrO_3$ exhibits extremely high grain boundary resistivity and has attracted extensive studies due to its electrical and optical properties [24,25]. $BaZrO_3$ materials have high chemical stability, high fusion temperature, and wide bandgap, which make them useful in various applications, such as in wireless communication systems components, field emission displays, plasma displays, and green photo-catalysis [26–30]. In addition, $BaZrO_3$ is an alternative material for yttria-stabilized zirconia as a thermal barrier coating material in the aerospace industry for supersonic jets [31]. Among the $AZrO_3$ (A: Ca, Sr or Ba) perovskites-type catalysts, $BaZrO_3$ shows significantly high catalytic activity and high proton conductivity, which makes acceptor-doped $BaZrO_3$ a potential candidate for use in applications such as hydrogen sensors, SOFCs electrolytes, and H_2

* Corresponding author.
E-mail address: vijayjiin2006@yahoo.com (V. Singh).

https://doi.org/10.1016/j.mseb.2020.114971
Received 23 April 2019; Received in revised form 18 November 2020; Accepted 20 November 2020
Available online 14 December 2020
0921-5107/

production and extraction [32,33]. Perovskite oxide materials can be used for nuclear waste disposal [34].

The extensive study of RE-doped $BaZrO_3$ includes the crystal structure and luminescent properties of Eu^{3+}-doped $BaZrO_3$ [35], the hydrothermal synthesis of $BaZrO_3$:Eu hybrid nanotube arrays using ZrO_2 nanotube layers as a template with different Eu^{3+}-doped contents [36], the ferromagnetism and photoluminescence (PL) of multifunctional Fe-doped $BaZrO_3$ ceramics [37], the synthesis of visible light-emitting $BaZrO_3$ perovskite nanoceramics by an efficient, self-assisted, gel-combustion route [38], the use of Y-doped $BaZrO_3$ in intermediate temperature SOFCs as a proton-conducting solid electrolyte [39], the use of RE-activated $AZrO_3$ (A = Ba, Ca, Sr) phosphors for display and sensing [28], the electrochemical characterization and oxygen permeation properties of Fe-doped $BaZrO_3$ [40], the synthesis and photocatalytic characterization of a new photocatalyst, $BaZrO_3$ [41], the use of perovskite materials for highly efficient flexible photocatalyst [42–45], the visible frequency upconversion in Er^{3+} and Yb^{3+} co-doped $BaZrO_3$ phosphor [46], the oxidation number and coordination system of an actinide uranium ion in $SrZrO_3$ perovskite [47], and the luminescence properties of $A^{2+}B^{4+}O_3$ (A = Ba, Ca, Sr, and B = Ti, Zr, Si, Hf, etc.) perovskite-type oxides activated with lanthanide and actinide ions [48–54].

Ultraviolet-emitting luminescent systems UVA (315–400 nm), UVB (280–315 nm), and UVC (100–280 nm) have been widely applied in the field of developing phototherapy lamps, display devices, fluorescent lamps, and photochemistry [55–58]. Ultraviolet radiation from the sun is a source of vitamin D. UVB induces the production of vitamin D in the skin at the rates of up to 1000 IUs per minute. UVB and UVA have applications in treating more than 40 types of skin conditions and disorders. Specifically, to heal the several kinds of skin diseases, such as psoriasis, eczema, vitiligo, narrow-band ultraviolet B radiation is used [55–60].

A Gd^{3+}-activated system has been proven an ideal compound in germicidal applications because of its well-defined, narrow-band emissions in the UV-B region. Gd^{3+} ion-doped material gives a strong and narrow ultraviolet-B emission under excitation by UV–visible light because doped Gd^{3+} increases the intensity of the host system by forming defect centers in the host crystal lattice. Extensive investigation of a UVB-emitting, Gd^{3+}-activated system for a phototherapy lamp revealed its high sensitivity to electron paramagnetic resonance (EPR) spectroscopy [61–65]. This research background led us to investigate the EPR spectra of the Gd^{3+}-doped perovskite $BaZrO_3$ host system synthesized by sol-gel technique.

EPR is an extremely sensitive method for detecting the existence of free radicals, as it can detect 10^{13} spins. Furthermore, it is known that PL spectroscopy can be used to analyze the optical properties and local structures of the luminescent system. This is a convenient technique for estimating and detecting RE and transition metal ions at an ultra-trace level in solids. Therefore, herein we have used these techniques and other techniques for materials characterization to investigate the structure, paramagnetic centers, and optical property correlation of $BaZrO_3$ with different Gd^{3+} doping levels.

2. Materials and methods

The $BaZrO_3$:xGd^{3+} ($x = 0.01 \leq x \leq 0.11$) samples were synthesized by a simple sol-gel method using high purity of $ZrO(NO_3)_2{\cdot}2H_2O$, $Ba(NO_3)_2$, citric acid, and $Gd(NO_3)_3{\cdot}6H_2O$ as starting materials, as shown in Table 1. In a typical synthesis, a stoichiometric amount of metal nitrates was dissolved in 10 ml deionized water in a 100 ml glass beaker. Citric acid (citric acid/metal ion = 2:1, molar ratio) was added as a chelating agent with continuous stirring to obtain a homogeneous solution that was kept at 115 °C overnight in an oven to obtain the dried gel. This dried gel was then fired in a furnace at 410 °C for 2 h. The obtained residual was crushed and calcined at 1055 °C for 4 h to get the final product.

The crystalline phase of the synthesized materials was characterized by X-ray diffraction (XRD; RIGAKU Miniflex-II diffractometer) using CuKα radiation (λ = 1.5406 Å). The measured XRD patterns were performed at a scan rate of 5°/min in the range of 10–80°. The surface morphology was obtained by scanning electron microscopy (SEM; S-3400, Hitachi, Japan). The room temperature (RT) excitation spectra and emission were recorded using a Shimadzu RF-5301PC spectrofluorophotometer with a xenon lamp as an excitation source. The same amount of sample was used while recording the PL spectra. Excitation and emission spectra were recorded with a spectral slit width of 1.5 nm. The EPR spectra of the sample were recorded on a JEOL FE1X ESR Spectrometer, operating in the X-band frequencies, using the conventional 100 kHz magnetic field modulation.

Table 1
Detailed information of sample composition and starting materials.

Sample composition	Base materials			
$BaZrO_3$: $Gd_{0.01}$	Ba = 1.0452 g	Zr = 1.0688 g	C. A = 3.0736 g	Gd = 0.0180 g
$BaZrO_3$: $Gd_{0.03}$	Ba = 1.0452 g	Zr = 1.0688 g	C. A = 3.0736 g	Gd = 0.0541 g
$BaZrO_3$: $Gd_{0.05}$	Ba = 1.0452 g	Zr = 1.0688 g	C. A = 3.0736 g	Gd = 0.0902 g
$BaZrO_3$: $Gd_{0.07}$	Ba = 1.0452 g	Zr = 1.0688 g	C. A = 3.0736 g	Gd = 0.1263 g
$BaZrO_3$: $Gd_{0.09}$	Ba = 1.0452 g	Zr = 1.0688 g	C. A = 3.0736 g	Gd = 0.1624 g
$BaZrO_3$: $Gd_{0.11}$	Ba = 1.0452 g	Zr = 1.0688 g	C. A = 3.0736 g	Gd = 0.1985 g

Ba = $Ba(NO_3)_2$, Zr = $ZrO(NO_3)_2{\cdot}2H_2O$, C.A = Citric acid, Gd = $Gd(NO_3)_3{\cdot}6H_2O$.

3. Results and discussion

3.1. Crystal structure and morphology

Fig. 1 displays the crystalline phase of $BaZrO_3$ and $BaZrO_3$:xGd^{3+} ($x = 0.01 \leq x \leq 0.11$). The diffraction peaks of all the samples correspond to a perovskite-type cubic structure, which agrees with the JCPDS No-06-0399. The $BaZrO_3$ ceramic was indexed as having cubic symmetry with the point joint-group symmetry O_h and space group of $Pm\bar{3}m$. The diffraction pattern shows that the sample contained some minor unknown impurity peaks around 26.27°, 33.62°, and 41.68° up to 0.03 mol of Gd^{3+} ions. A clear decreasing trend in impurity peaks is visible with increasing Gd^{3+} concentration beyond 0.03 mol. These results demonstrated that trivalent Gd^{3+} ions were dissolved in the $BaZrO_3$ host matrix without changing the structural prototype. However, the

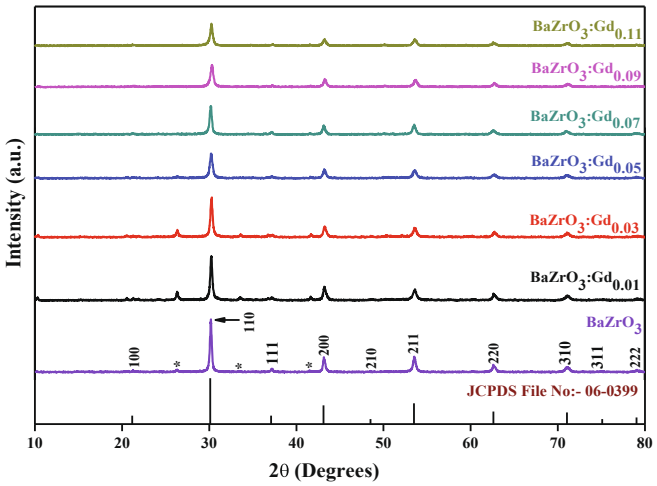

Fig. 1. XRD patterns of $BaZrO_3$:xGd^{3+} ($x = 0.01 \leq x \leq 0.11$) ceramic.

XRD peak intensity decreased with increasing Gd^{3+} concentration, possibly due to the change in electron density or to point defects. A study of the effects of dopant concentration in $BaZr_{1-x}Eu_xO_3$ ($x = 0.0 \leq x \leq 0.10$) phosphors found that XRD lines broaden with increasing x [66], which was partly attributed to the increased lattice defect and disorder formation induced by the doping. The study's XRD results indicated that in the above composition range, the Eu^{3+} ions substitute for Zr^{4+} sites without changing the crystal structure of cubic $BaZrO_3$. In another study of the influence of Er doping on the structural, optical, and luminescence properties of pulsed-laser-deposited Er: $BaZrO_3$ thin films [67], the XRD data revealed a decrease in d-spacing for all the doped films in comparison to pure $BaZrO_3$ film, which is suggestive of the compressive stress in films. Crystallite size was determined using the Scherrer equation, $D = 0.941\lambda/\beta\cos\theta$, where D is the average crystallite size, λ the X-ray wavelength, θ the Bragg diffraction angle, and β the line broadening at half the maximum intensity (FWHM). The calculated crystallite size (D) of this method ranged from 20 to 28 nm. The structures of previously reported $BaZrO_3$ show that a larger cation Ba is located at the center and bonded to twelve O atoms with a cuboctahedral configuration that forms [BaO_{12}] clusters. In comparison, smaller cation Zr is located at the corners and bonded to six oxygen (O) atoms, which form the octahedral [ZrO_6] clusters [68,69]. The doped Gd^{3+} ions can partially occupy the Ba and Zr cation sites [68,69].

The SEM images in Fig. 2 showing the surface morphology of $BaZrO_3$:0.07Gd powder at different magnifications reveal the size variation of the particles within the range of a few micrometers with no characteristic shape and merely a loose, foamy, irregular, and aggregated form (Fig. 2a and b). The particles' highly interconnected nature makes it difficult to predict their morphology. Random grain growth is visible, with an agglomeration of smaller particles forming the grains (Fig. 2c). The smaller particles are sintered together to form larger particles, which is ascribed to the high annealing temperature. Smaller particles are formed on the surface of bigger particles due to the liberation of heat in the form of gas during the annealing process (Fig. 2d).

3.2. Photoluminescence (PL) analysis

The PL excitation spectra of $BaZrO_3$:xGd^{3+} ($x = 0.01 \leq x \leq 0.11$) were investigated at RT with the emission monitored at 315 nm. Fig. 3 (a) displays the excitation spectra. The excitation spectra reveal several bands around 254, 275, and 277 nm in the UV region. The band near 254 nm is assigned to $^8S_{7/2} \rightarrow {}^6D_J$ transitions of Gd^{3+} ions [64,65]. The intense bands around 274 nm, 275 nm, and 276 nm are allocated to $^8S_{7/2} \rightarrow {}^6I_J$ transitions of Gd^{3+} ions [64,65]. An intense peak was reported around 275 nm in Gd^{3+}-doped barium-phosphate glasses when observing the $^6P_{7/2} \rightarrow {}^8S_{7/2}$ emission of Gd^{3+} at 315 nm [70]. Bands were observed at 230 nm, 258 nm, and 276 nm due to f–f transitions of the Gd^{3+} ion in aluminosilicate oxyfluoride glasses [71]. Fig. 3(b) shows the emission spectra of $BaZrO_3$:xGd^{3+} ($x = 0.01 \leq x \leq 0.11$) under an excitation wavelength of 275 nm. The emission spectrum exhibits an intense band around 315 nm and weak bands around 313 nm and 322 nm. These bands are caused by the transition from the excited state ^6P_J to the ground state $^8S_{7/2}$ of Gd^{3+} ions. An examination of Gd^{3+}-doped Y_2O_3 revealed emission bands at 314, 315, and 322 nm under X-ray excitation [72]. The sharp emission band at 314 nm in Gd^{3+}-doped $YAlO_3$ epitaxial thin films corresponded to $^6P_J \rightarrow {}^8S_{7/2}$ transition of Gd^{3+} ions [73]. Fig. 4 displays the energy level diagram of Gd^{3+}. In $BaZrO_3$, Gd^{3+} emission mainly occurs at 315 nm. Upon 275 nm excitation, Gd^{3+} ions are excited to the ^6D_J and ^6I_J levels, then decay non-radiatively to the ^6P_J state, and finally are radiatively relaxed from ^6P_J to $^8S_{7/2}$ to give an emission at 315 nm in the UVB region. PL studies show the usefulness of the synthesized phosphors in phototherapy lamp for treating skin diseases.

Fig. 5 shows that the emission intensity of $BaZrO_3$:xGd^{3+}

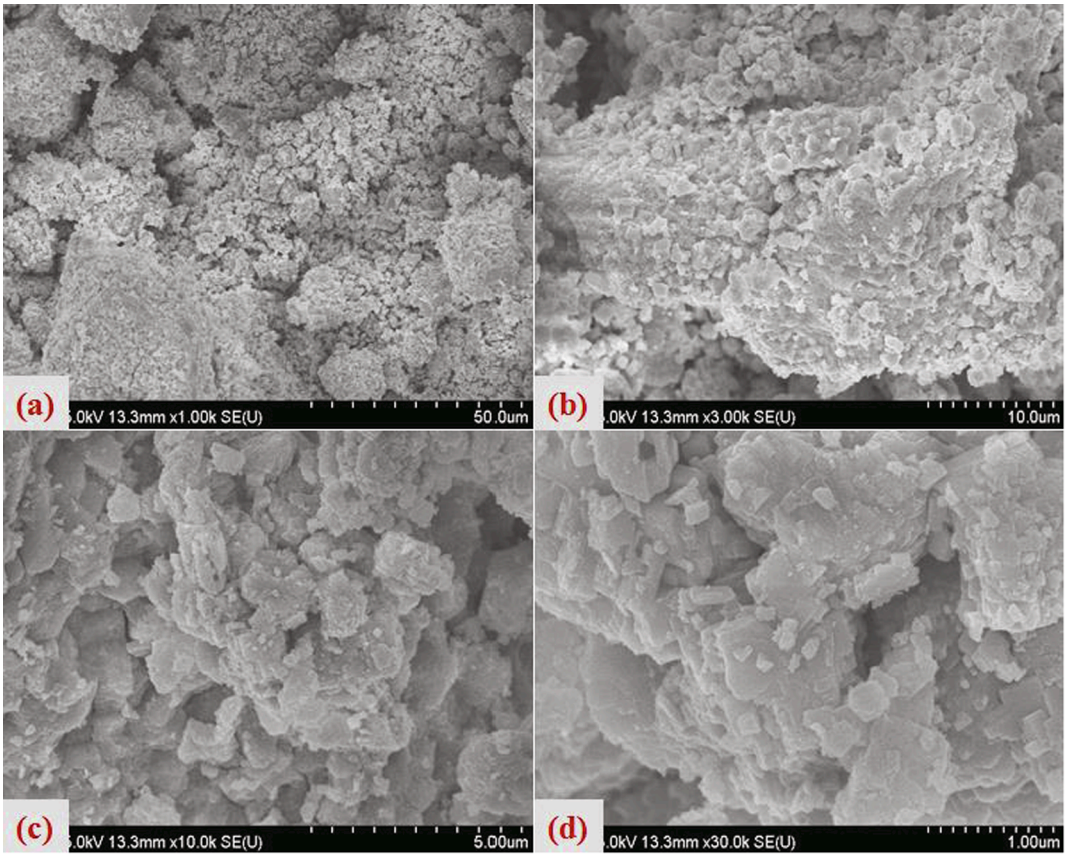

Fig. 2. SEM images of $BaZrO_3$:$Gd_{0.07}$ ceramic.

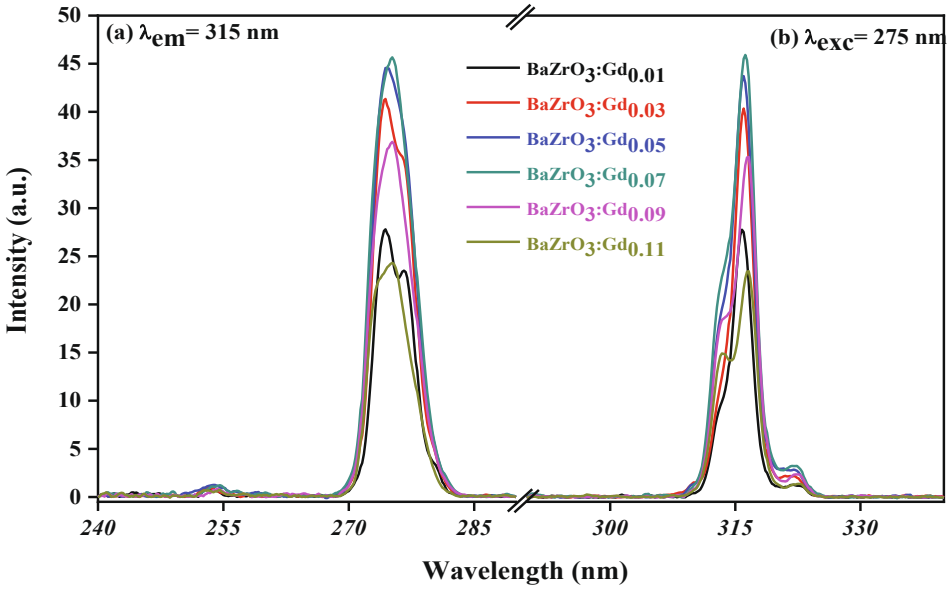

Fig. 3. Photoluminescence spectra of $BaZrO_3$:xGd^{3+} ($x = 0.01 \leq x \leq 0.11$) ceramic (a) Excitation spectrum of $BaZrO_3$:xGd^{3+} ($x = 0.01 \leq x \leq 0.11$) ($\lambda_{em} = 315$ nm) and (b) Emission spectrum of $BaZrO_3$:xGd^{3+} ($x = 0.01 \leq x \leq 0.11$) ($\lambda_{exc} = 275$ nm).

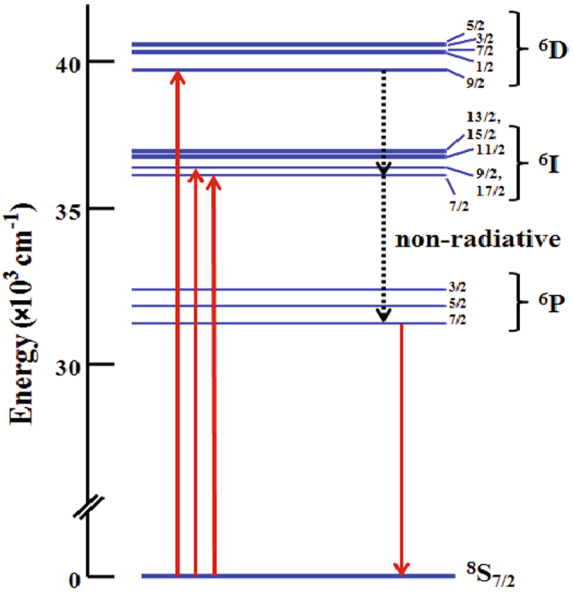

Fig. 4. The energy level diagram of Gd^{3+} ions.

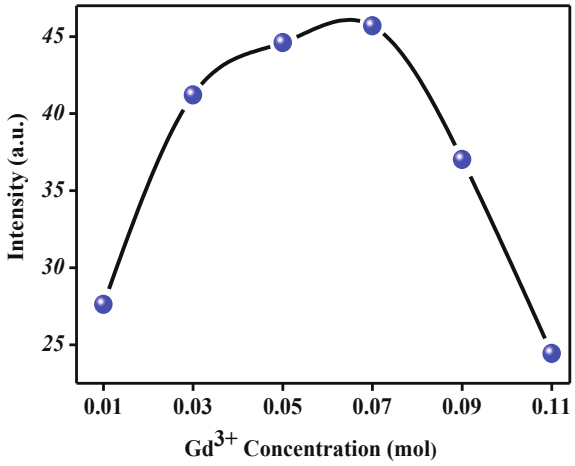

Fig. 5. Variation in the emission intensity of 315 nm peak as a function of Gd^{3+} concentration.

($x = 0.01 \leq x \leq 0.11$) changes with the doping concentration of Gd^{3+} ions. The emission intensity of the sample initially increases with increasing Gd^{3+} concentration. As the distance between two adjacent Gd^{3+} ions is decreased by increasing Gd^{3+} concentration, the interaction between Gd^{3+}- Gd^{3+} ions is enhanced, leading to nonradiative energy transfer between two Gd^{3+} ions. The electric multipolar and exchange interactions are involved in energy transfer. In the present system, the emission peaks at $x = 0.07$, which is the critical concentration, due to the concentration quenching effect arising from non-radiative energy transfer processes (cross-relaxation) among Gd^{3+} ions because of multipole–multipole interactions or exchange interaction [74]. Confirming the type of interaction mechanism requires determination of the critical separation distance between the acceptor and donor, as defined by Blasse's equation, which is used to calculate the critical energy transfer distance (R_c) through concentration quenching:

$$R_c \approx 2\left[\frac{3V}{4\pi\chi_c N}\right]^{1/3}$$

where V is the volume of the crystallographic unit cell of $BaZrO_3$ (73.1 Å^3) [75], χ_c the critical Gd^{3+} concentration, and N the number of Z ions in the unit cell (4). The energy transfer of the non-radiative critical distance is about to 8 Å. The estimated R_c value is 8 Å, which is bigger than the 5 Å for exchange interaction; therefore, multipolar interaction is responsible for the energy transfer between the nearest-neighbor ions. To check the oxidation state of fused Gd^{3+} ions species, they were subjected to EPR studies, as described below.

3.3. Electron paramagnetic resonance (EPR) analysis

Fig. 6 shows the EPR spectrum of undoped $BaZrO_3$ recorded at RT. A high-intensity signal is observed in the free-electron region ($g \sim 2.0023$). Fig. 7 illustrates the expanded spectrum focusing on the free-electron region. We attributed the spectrum to two different centers: one characterized by an axially symmetric g-tensor and the other with an

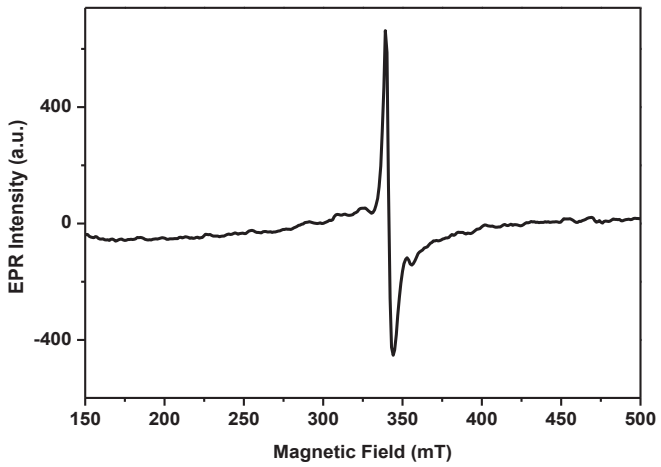

Fig. 6. Room temperature electron paramagnetic resonance (EPR) spectrum of un-doped $BaZrO_3$ ceramic.

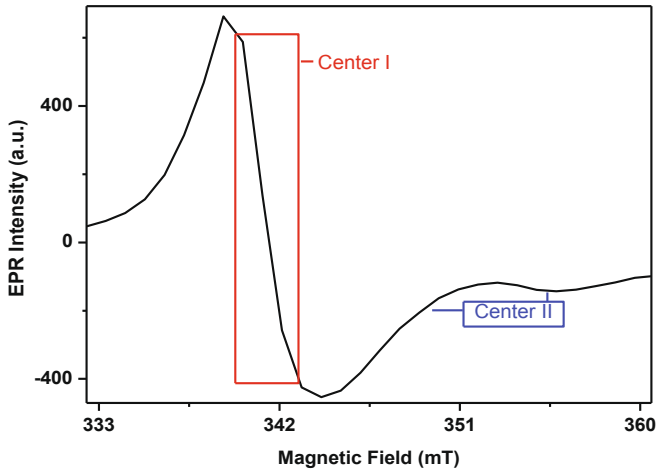

Fig. 7. Electron paramagnetic resonance (EPR) spectrum at room temperature of $BaZrO_3$ in the free-electron region ($g \sim 2.0023$). Center I line is assigned to an F^+-center, and center II, characterized by an axial g-tensor, is ascribed to a Zr^{3+} ion.

isotropic g-value. The EPR lines corresponding to these two centers are designated in Fig. 7.

$BaZrO_3$ is a perovskite of the ABO_3 family and the oxygen ions with Zr^{4+} ion sited at the center of the octahedron [76]. A three-dimensional framework is formed by linking these octahedra by sharing corners. On the other hand, Ba^{2+} ions are coordinated by oxygen ions which form a cubo-octahedral coordination. The $BaZrO_3$ lattice contains divalent Ba^{2+} ions and tetravalent Zr^{4+} ions. Hence, a partial substitution of tetravalent ions by divalent ions is possible as a consequence of anti-site cation exchange. This type of substitution is a point defect in crystals that is termed cation exchange disorder. Truong et al. [77] have directly observed this disorder in crystal lattices.

Fig. 7 shows the Center I characterized by a g-value equal to 1.973 and a linewidth of 48 Gauss. The EPR line has a relatively large linewidth, such as arises in the presence of an unresolved hyperfine structure that can be induced by the interaction of the unpaired electron with near by nuclear spins. In the present $BaZrO_3$ system, barium and zirconium have isotopes with nuclear spins. ^{135}Ba and ^{137}Ba are barium isotopes with nuclear spin 3/2 [78]. The abundance of ^{135}Ba (11.2%) is more than ^{137}Ba (6.6%). The nuclear magnetic moment of ^{137}Ba (0.94) is higher than ^{135}Ba (0.84). ^{91}Zr has an abundance of 11.2% with nuclear spin 5/2 and a magnetic moment of −1.3 [78]. Therefore, the unpaired electron interacts with both barium and zirconium nuclear spins.

Cation exchange disorder mentioned earlier, and non-stoichiometry leads to lattice defects resulting in trapping centers. It has been shown by first-principle calculations [79] that oxygen vacancies can form in crystal lattices with cation disorder. These vacancies can trap electrons during irradiation and can result in the formation of F^+-centers (an electron trapped at an anion vacancy). Such centers can form in a system like $BaZrO_3$. The amount of delocalization of the unpaired electrons, along with magnetic moments and relative abundance of isotopes of ions present in the system, determine the linewidth.

The main feature of an F-center is a g-value near to the free-electron value and a g-shift, which may be positive or adverse. In the $BaZrO_3$ system, center I has a slight g-shift and a large linewidth of 48 Gauss. Because of these observations, we tentatively assigned center I as an F^+-center. The aforementioned oxygen vacancies present in the system trap electrons during the preparation of the phosphor, which induces the formation of the F^+-center. Defect centers are formed when phosphors are subjected to ionizing radiation. However, the $BaZrO_3$ system seems to be a special case where defect centers are formed most probably during the preparation of the ceramic powder. Another example, $YAlO_3$ (Yttrium-aluminum) perovskite was grown in vacuum [80].

The second center observed in undoped $BaZrO_3$ (center II) has an axially symmetric g-tensor with principal values $g_{\|} = 1.895$ and $g_{\perp} = 1.978$. A center that may be observed in systems with zirconium ions in the Zr^{3+} ion observed recently in pure polycrystalline zirconia and in zirconium subjected to reductive treatments too [81]. The Zr^{3+} ion is characterized by the principal g-values $g_{\|} = 1.959$ and $g_{\perp} = 1.977$ in this system. This center is also observed in other systems like ZrF_4 [82], Zr-doped YPO_4 [83], and Zr-doped YAG [84]. These studies showed that the center has g-values lower than the free-electron value (2.0023) when the ion is located in lower symmetry environments like a distorted cube or distorted octahedral sites and also $g_{\|} < g_{\perp}$.

Center II in $BaZrO_3$ has an axial g-tensor with principal values less than the free-electron value. Based on the previous studies of the Zr^{3+} ion, center II in the current system is tentatively identified as the Zr^{3+} ion. The crystal structure indicates that zirconium ion is situated in a regular octahedron environment in $BaZrO_3$ [76]. The oxygen vacancies existing in the lattice due to anti-site disorder could cause changes in the zirconium ion's environment, leading to a lower symmetry. The deviation from the regular octahedral environment could cause the g-tensor to exhibit axial symmetry.

Fig. 8 displays the EPR spectrum observed at RT in Gd^{3+}-doped $BaZrO_3$. This signal is ascribed to a Gd^{3+} ion, which likely experiences a poor crystal field arising from the Gd^{3+} lattice site. Brodbeck and Iton explained the EPR spectrum of Gd^{3+} ion in powder systems [85], and

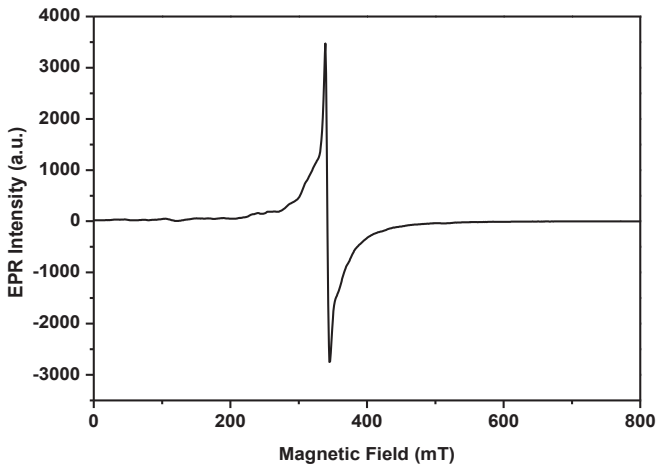

Fig. 8. Electron paramagnetic resonance (EPR) spectrum of $BaZrO_3$:Gd^{3+} at room temperature.

also proposed that Gd^{3+} ion limited with the poor crystal and located in a comparatively undistorted environment displays EPR lines near the $g \sim 2.0$ region. On the other hand, Gd^{3+} ion experiences a strong crystal field (according to the Brodbeck and Iton representation if it is an intermediate crystal field) in a distorted environment, and low field lines are now seen in the ESR spectrum.

Ionic radii considerations suggest that the Gd^{3+} ion is likely to be located at the Zr^{4+} site in $BaZrO_3$. The Zr^{4+} ion in an octahedral coordination has an ionic radius of 0.72 Å [86]. Ba^{2+} ion has 12-fold coordination and an ionic radius of 1.61 Å. In the 6-fold coordination of an octahedron, the ionic radius of Gd^{3+} is 0.94 Å, compared to 1.11 Å in the 9-fold coordination. The Pr^{4+} ion with an ionic radius (0.85 Å) close to the 6-fold coordination of Gd^{3+} ion has previously been found on the Zr^{4+} site [87].

However, another study on $BaTiO_3$, a system very similar to $BaZrO_3$, showed that Gd^{3+} ion replaces Ba^{2+} ion [88]. Therefore, Gd^{3+} ion can be located at Zr^{4+} sites and at Ba^{2+} sites in the $BaZrO_3$:Gd ceramic. A careful examination of the observed spectra indicates that it is a superposition of two lines with almost identical g-values but differing linewidths. An expanded view of the spectrum showing the central EPR line is shown in Fig. 9. The linewidth of one of the lines is 86 Gauss [Gd^{3+}(1)] whilst the other line [Gd^{3+}(2)] has a broader linewidth of 296 Gauss. The *g*-value is 1.94 for both lines. We believe that these two lines originate from the Gd^{3+} ion situated at the Zr^{4+} and Ba^{2+} sites in the lattice. Fig. 10 displays the observed EPR spectrum with an increase of Gd^{3+} ions concentration. The intensity of the narrow Gd^{3+} line is almost constant with increasing Gd^{3+} content in the phosphor. However, the broad Gd^{3+} line has a smaller intensity at a dopant concentration of 0.01 mol. The intensity of the broad Gd^{3+} line increases with increasing dopant concentration and reaches saturation at about 0.07 mol Gd^{3+} concentration. The Gd^{3+} ion appears to prefer occupying the site, giving rise to a broad line when the dopant concentration increases.

Charge neutrality requires Ba^{2+} vacancies to be created when Gd^{3+} ions replace Ba^{2+} ions. The presence of vacancies near the Gd^{3+} site can change the environment around the Gd^{3+} ion and thereby induce distortions near the Gd^{3+} site and increase the crystal field experienced by the ion. Brodbeck and Iton et al. [85] suggested that the lines would be seen in the low field region of the spectrum at a stronger crystal field. However, Gd^{3+} lines are seen near the $g \sim 2.0$ region, indicating that the charge compensator is located farther from the Gd^{3+} site. When Gd^{3+} ions substitute for Zr^{4+} ions, oxygen vacancies are created for charge compensation.

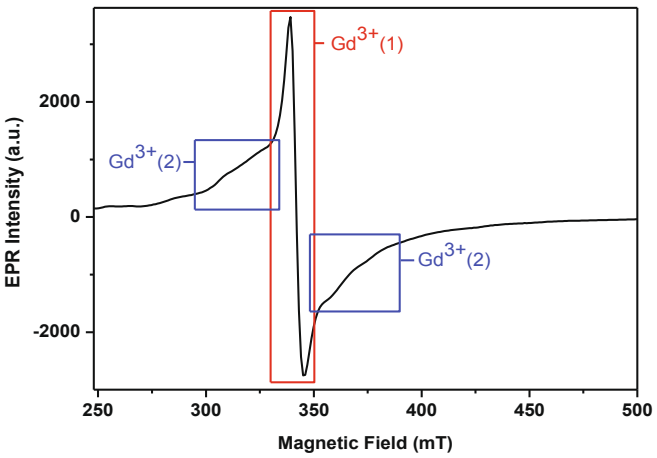

Fig. 9. Expanded view of electron paramagnetic resonance (EPR) spectrum of $BaZrO_3$:Gd^{3+} at room temperature.

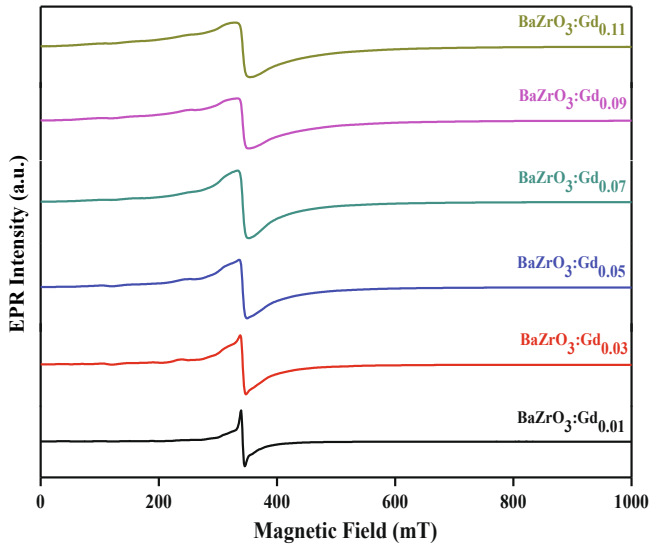

Fig. 10. Electron paramagnetic resonance (EPR) spectra of $BaZrO_3$:xGd^{3+} ($x = 0.01 \leq x \leq 0.11$) ceramic.

4. Conclusions

In summary, we demonstrated that the undoped and Gd^{3+}-doped $BaZrO_3$ ceramic with a perovskite structure can be effectively prepared by the sol-gel method. Among the detailed characterization analyses, the XRD results revealed the disappearance of very low-intensity impurity peaks at a high doping level of more than 0.03 mol. Correspondingly, increasing the Gd^{3+} concentration decreased the XRD peaks intensity. The SEM data revealed the ceramic's irregular morphology and high degree of aggregation. The emission band near 315 nm was assigned to $^6P_{7/2} \rightarrow {}^8S_{7/2}$ transition of the Gd^{3+} ion, upon excitation at 275 nm. The $BaZrO_3$:Gd^{3+} ceramic prepared with a Gd^{3+} concentration of 0.07 mol showed the maximum emission intensity. The PL results demonstrated the ceramic's attractive luminescence property for the generation of UVB-emitting radiation. The prepared ceramic exhibited EPR lines due to defect centers probably formed during the synthesis. These were tentatively identified as F^+- center and Zr^{3+} ion. A relatively high symmetry environment around the Gd^{3+} ion was indicated by the gadolinium-doped ceramic's EPR lines near the $g \sim 2.0$ region. The Gd^{3+} ion appeared to be located at both the Zr^{4+} sites and the Ba^{2+} sites.

Declaration of Competing Interest

The authors declare that they have no known competing financial interests or personal relationships that could have appeared to influence the work reported in this paper.

Acknowledgements

This work was supported by the National Research Foundation of Korea (NRF) grant funded by the Korea government (MSIT) (2018M2B2A9065656).

References

[1] B.A. Hernandez, K.S. Chang, E.R. Fisher, P.K. Dorhout, Sol-gel template synthesis and characterization of $BaTiO_3$ and $PbTiO_3$ nanotubes, Chem. Mater. 14 (2002) 480–482.
[2] S. Nakayama, $LaFeO_3$ perovskite-type oxide prepared by oxide-mixing, co-precipitation and complex synthesis methods, J. Mater. Sci. 36 (2001) 5643–5648.
[3] Y. Li, S. Yao, W. Wen, L. Xue, Y. Yan, Sol-gel combustion synthesis and visible-light-driven photocatalytic property of perovskite $LaNiO_3$, J. Alloys Compd. 491 (2010) 560–564.

[4] J.Y. Choi, C.H. Kim, D.K. Kim, Hydrothermal synthesis of spherical perovskite oxide powders using spherical gel powders, J. Am. Ceram. Soc. 81 (1998) 1353–1356.

[5] J. Spooren, A. Rumplecker, F. Millange, R.I. Walton, Subcritical hydrothermal synthesis of perovskite manganites: a direct and rapid route to complex transition-metal oxides, Chem. Mater. 15 (2003) 1401–1403.

[6] R. Shi, J. Liu, H. Wang, F. Wu, H. Miao, Intermediate temperature fuel cell durability of Eu-doped $SrCeO_3$-$SrZrO_3$ solid solution/ NaCl-KCl composite electrolyte, Ceram. Int. 43 (2017) 16931–16935.

[7] S.G.P. Kumar, R.H. Krishna, N. Kottam, P.K. Murthy, C. Manjunatha, R. Preetham, C. Shivakumara, T. Thomas, Understanding the photoluminescence behaviour in nano $CaZrO_3$:Eu^{3+} pigments by Judd-Ofelt intensity parameters, Dyes Pigm. 150 (2018) 306–314.

[8] W.D. Macedo Jr, A.E. Souza, G.T.A. Santos, S.R. Teixeira, E. Longo, Microwave-assisted hydrothermal synthesis followed by heat treatment: a new route to obtain $CaZrO_3$, Ceram. Int. 44 (2018) 953–958.

[9] Z. Barandiarán, M. Bettinell, L. Seijo, Color control of Pr^{3+} luminescence by electron-hole recombination energy transfer in $CaTiO_3$ and $CaZrO_3$, J. Phys. Chem. Lett. 8 (2017) 3095–3100.

[10] A. Lindman, T.S. Bjørheim, G. Wahnström, Defect segregation to grain boundaries in $BaZrO_3$ from first-principles free energy calculations, J. Mater. Chem. A 5 (2017) 13421–13429.

[11] N.A. Noor, Q. Mahmood, M. Hassan, A. Laref, M. Rashid, Physical properties of cubic $BaGeO_3$ perovskite at various pressure using first-principle calculations for energy renewable devices, J. Mol. Graph. 84 (2018) 152–159.

[12] M. Saliba, J.P. Correa-Baena, M. Grätzel, A. Hagfeldt, A. Abate, Perovskite solar cells: from the atomic level to film quality and device performance, Angew. Chem. Int. Ed. 57 (2018) 2554–2569.

[13] J. Sunarso, S.S. Hashim, N. Zhu, W. Zhou, Perovskite oxides applications in high temperature oxygen separation, solid oxide fuel cell and membrane reactor: a review, Prog. Energy Combust. Sci. 61 (2017) 57–77.

[14] F. Li, Z. Xia, Y. Gong, L. Gu, Q. Liu, Optical properties of Mn^{2+} doped cesium lead halide perovskite nanocrystals via a cation-anion co-substitution exchange reaction, J. Mater. Chem. C 5 (2017) 9281–9287.

[15] S.Y. Liu, Y. Meng, S. Liu, D.J. Li, Y. Li, Y. Liu, Y. Shen, S. Wang, Phase stability, electronic structures, and superconductivity properties of the $BaPb_{1-x}Bi_xO_3$ and $Ba_{1-x}K_xBiO_3$ perovskites, J. Am. Ceram. Soc. 100 (2017) 1221–1230.

[16] C. Sasikala, N. Durairaj, I. Baskaran, B. Sathyaseelan, M. Henini, E. Manikandan, Transition metal titanium (Ti) doped $LaFeO_3$ nanoparticles for enhanced optical structural and magnetic properties, J. Alloys Compd. 712 (2017) 870–877.

[17] C. Duan, D. Hook, Y. Chen, J. Tong, R. O'Hayre, Zr and Y co-doped perovskite as a stable, high performance cathode for solid oxide fuel cells operating below 500°C, Energy Environ. Sci. 10 (2017) 176–182.

[18] Z. Pan, Q. Liu, L. Zhang, J. Zhou, C. Zhang, S.H. Chan, Experimental and thermodynamic study on the performance of water electrolysis by solid oxide electrolyzer cells with Nb-doped Co-based perovskite anode, Appl. Energy 191 (2017) 559–567.

[19] I. Jaouali, H. Hamrouni, N. Moussa, M.F. Nsib, M.A. Centeno, A. Bonavita, G. Neri, S.G. Leonardi, $LaFeO_3$ ceramics as selective oxygen sensors at mild temperature, Ceram. Int. 44 (2018) 4183–4189.

[20] F. Gunkel, L. Jin, D.N. Mueller, C. Hausner, D.S. Bick, C.-L. Jia, T. Schneller, I. Valvov, R. Waser, R. Dittmann, Ordering and phase control in epitaxial double-perovskite catalysts for the oxygen evolution reaction, ACS Catal. 7 (2017) 7029–7037.

[21] I.-M. Hung, Y.-J. Chiang, Y.-H. Wang, J.S.C. Jang, S.-W. Lee, Electrical properties and hydrogen flux performance of $Sr(Ce_{0.6}Zr_{0.4})_{1-x}Y_xO_{3-\delta}$ ceramic proton conductors, Int. J. Hydrog. Energy 42 (2017) 22149–22158.

[22] D.K. Singh, K. Mondal, J. Manam, Improved photoluminescence, thermal stability and temperature sensing performances of K^+ incorporated perovskite $BaTiO_3$:Eu^{3+} red emitting phosphors, Ceram. Int. 43 (2017) 13602–13611.

[23] R. Phatak, A.K. Yadav, N. Pathak, C.L. Prajapat, U.M. Kasar, M.R. Singh, S.N. Jha, D. Bhattacharyya, A. Das, S.K. Sali, Pentavalent uranium complex oxides: a case study on double perovskites $Ba_2REU^{5+}O_6$ (RE = La, Nd, Sm), J. Alloys Compd. 708 (2017) 1168–1177.

[24] Y. Liu, W. Zhang, B. Wang, L. Sun, F. Li, Z. Xue, G. Zhou, B. Liu, H. Nian, Theoretical and experimental investigations on high temperature mechanical and thermal properties of $BaZrO_3$, Ceram. Int. 44 (2018) 16475–16482.

[25] A. Lindman, E.E. Helgee, G. Wahnström, Comparison of Space-charge formation at grain boundaries in proton-conducting $BaZrO_3$ and $BaCeO_3$, Chem. Mater. 29 (2017) 7931–7941.

[26] X. Yang, Y. Wang, Q. Song, Y. Chen, Y.H. Xue, Pressure effects on structural, electronic, elastic, and optical properties of cubic and tetragonal phases of $BaZrO_3$, Acta Phys. Pol. A 133 (2018) 1138–1143.

[27] L. Bi, E. Traversa, Synthesis strategies for improving the performance of doped-$BaZrO_3$ materials in solid oxide fuel cell applications, J. Mater. Res. 29 (2014) 1–15.

[28] S. Tripathi, R. Tiwari, A.K. Shrivastava, V.K. Singh, N. Dubey, V. Dubey, A review reports on rare earth activated $AZrO_3$ (A=Ba, Ca, Sr) phosphors for display and sensing applications, Optik 157 (2018) 365–381.

[29] L. Wang, M. Habibi, J.I. Eldridge, S. Guo, Infrared radiative properties of plasma-sprayed $BaZrO_3$ coatings, J. Eur. Ceram. Soc. 34 (2014) 3941–3949.

[30] M.L. Moreira, D.P. Volanti, J. Andrés, P.J. Montes, M.E. Valerio, J.A. Varela, E. Longo, Radioluminescence properties of decaoctahedral $BaZrO_3$, Scr. Mater. 64 (2011) 118–121.

[31] A.C. Karaoglanli, K.M. Doleker, Y. Ozgurluk, State of the art thermal barrier coating (TBC) materials and TBC failure mechanisms, in: A. Öchsner, H. Altenbach, (Eds.), properties and characterization of modern materials. Advanced Structured Materials, 33. Springer, Singapore, 2017, pp. 441–452.

[32] N. Shimoda, Y. Kimura, Y. Kobayashi, J. Kubota, S. Satokawa, Ammonia synthesis over yttrium-doped barium zirconate and cerate-based perovskite-type oxide supported ruthenium catalysts, Int. J. Hydrog. Energy. 42 (2017) 29745–29755.

[33] T. Charoonsuk, N. Vittayakorn, Soft-mechanochemical synthesis of monodispersed $BaZrO_3$ sub-microspheres: phase formation and growth mechanism, Mater. Design. 118 (2017) 44–52.

[34] G.R. Lumpkin, Alpha-decay damage and aqueous durability of actinide host phase in natural system, J. Nucl. Mater. 289 (2001) 136–166.

[35] G. Li, J. Litao, G. Shuqing, L. Yunfeng, L. Xu, G. Qinglin, Y. Zhiping, F. Guangsheng, Luminescent properties of Eu^{3+}-doped $BaZrO_3$ phosphor for UV white light emitting diode, J. Rare Earths 28 (2010) 292–294.

[36] L. Guo, X. Wang, C. Zhong, L. Li, Preparation and photoluminescence properties of Eu^{3+}-doped $BaZrO_3$ nanotube arrays, J. Am. Ceram. Soc. 94 (2011) 3175–3177.

[37] P.P. Khirade, S.D. Birajdar, A.B. Shinde, K.M. Jadhav, Room temperature ferromagnetism and photoluminescence of multifunctional Fe doped $BaZrO_3$ nanoceramics, J. Alloys Compd. 691 (2017) 287–298.

[38] S.K. Gupta, N. Pathak, R.M. Kadam, An efficient gel-combustion synthesis of visible light emitting barium zirconate perovskite nanoceramics: probing the photoluminescence of Sm^{3+} and Eu^{3+} doped $BaZrO_3$, J. Lumin. 169 (2016) 106–114.

[39] R.B. Cervera, Y. Oyama, S. Miyoshi, K. Kobayashi, T. Yagi, S. Yamaguchi, Structural study and proton transport of bulk nanograined Y-doped $BaZrO_3$ oxide protonics materials, Solid State Ion. 179 (2008) 236–242.

[40] H. Zhang, A. Suresh, C.B. Cater, B.A. Wilhite, Materials synthesis, electrochemical characterization and oxygen permeation properties of Fe-doped $BaZrO_3$, Solid State Ion. 266 (2014) 58–67.

[41] Y. Yuan, X. Zhang, L. Liu, X. Jiang, J. Luv, Z. Li, Z. Zou, Synthesis and photocatalytic characterization of a new photocatalyst $BaZrO_3$, Int. J. Hydrog. Energy 21 (2008) 5941–5946.

[42] Y. Huang, Z. Guo, H. Liu, S. Zhang, P. Wang, J. Lu, Y. Tong, Heterojunction architecture of N-Doped WO_3 nanobundles with Ce_2S_3 nanodots hybridized on a carbon textile enables a highly efficient flexible photocatalyst, Adv. Funct. Mater. 29 (2019), 190349.

[43] K. Li, X. Lu, Y. Zhang, K. Liu, Y. Huang, H. Liu, Bi_3TaO_7/Ti_3C_2 heterojunctions for enhanced photocatalytic removal of water-borne contaminants, Environ. Res. 185 (2020), 109409.

[44] K. Ye, K. Li, Y. Lu, Z. Guo, N. Ni, H. Liu, Y. Huang, H. Ji, P. Wang, An overview of advanced methods for the characterization of oxygen vacancies in materials, Trends Analyt Chem. 116 (2019) 102–108.

[45] K. Ye, Y. Li, H. Yang, M. Li, Y. Huang, S. Zhang, H. Ji, An ultrathin carbon layer activated CeO_2 heterojunction nanorods for photocatalytic degradation of organic pollutants, Appl. Catal. B 259 (2019), 118085.

[46] V. Singh, V.K. Rai, K. Al-Shamery, M. Haase, S.H. Kim, NIR to visible frequency upconversion in Er^{3+} and Yb^{3+} co-doped $BaZrO_3$ phosphor, Spectroc. Acta Part A 108 (2013) 141–145.

[47] S.K. Gupta, N. Pathak, R. Gupta, S.K. Thulasidas, V. Natarajan, Probing the oxidation state and coordination geometry of uranium ion in $SrZrO_3$ perovskite, J. Mol. Struct. 1068 (2014) 204–209.

[48] M. Dhanalakshmi, H. Nagabhushana, G.P. Darshan, R.B. Basavaraj, B. Daruka Prasad, Sonochemically assisted hollow/solid $BaTiO_3$:Dy^{3+} microspheres and their applications in effective detection of latent fingerprints and lip prints, J. Sci.: Adv. Mater. Dev. 2 (2017) 22–33.

[49] H. Wang, N. Yoshikawa, S. Yoshikado, T. Aruga, Mutually pumped phase conjugator with a rainbow configuration in $BaTiO_3$:Ce crystal using nanosecond pulses, Opt. Lett. 21 (1996) 561–563.

[50] H. Rétot, A. Bessière, A. Kahn-Harari, B. Viana, Synthesis and optical characterization of $SrHfO_3$:Ce and $SrZrO_3$:Ce nanoparticles, Opt. Mater. 30 (2008) 1109–1114.

[51] Y. Jin, Y. Hu, L. Chen, X. Wang, G. Ju, Z. Mou, Luminescence properties of dual-emission (UV/Visible) long afterglow phosphor $SrZrO_3$:Pr^{3+}, J. Am. Ceram. Soc. 96 (2013) 3821–3827.

[52] S.K. Gupta, A.K. Yadav, D. Bhattacharya, S.N. Jha, V. Natrajan, Visible light emitting Ln^{3+} ion (Ln=Sm, Eu and Dy) as a structural probe: a case study with $SrZrO_3$, J. Lumin. 164 (2015) 1–22.

[53] H. Li, Y. Zhang, L. Shao, P. Yuan, X. Xia, Influence of pump power and doping concentration for optical temperature sensing based on $BaZrO_3$:Yb^{3+}/Ho^{3+} ceramics, J. Lumin. 192 (2017) 999–1003.

[54] V. Singh, S. Watanabe, T.K. Gundu Rao, K. Al-Shamery, M. Haase, Y.-D. Jho, Synthesis, characterisation, luminescence and defect centres in solution combustion synthesised $CaZrO_3$:Tb^{3+} phosphor, J. Lumin. 132 (2012) 2036–2042.

[55] P.P. Mokoena, I.M. Nagpure, V. Kumar, R.E. Kroon, E.J. Olivier, J.H. Neethling, H. C. Swart, O.M. Ntwaeaborw, Enhanced UVB emission and analysis of chemical states of $Ca_5(PO_4)_3OH$:Gd^{3+}, Pr^{3+} phosphor prepared by co-precipitation, J. Phys. Chem. Solids 75 (2014) 998–1003.

[56] S. Tamboli, B. Rajeswari, S.J. Dhoble, Investigation of UV-emitting Gd^{3+}-doped $LiCaBO_3$ phosphor, J. Lumin. 31 (2016) 551–556.

[57] S. Dogra, A.J. Kanwar, Narrow band UVB phototherapy in dermatology, Indian J. Dermatol. Venereol. Leprol. 70 (2004) 205–209.

[58] A.O. Chauhan, N.S. Bajaj, S.K. Omanwar, Synthesis and photoluminescence study of narrow-band UVB-emitting $LiSr_4(BO_3)_3$:Gd^{3+}, Pr^{3+} phosphor, Bull. Mater. Sci. 40 (2017) 1–6.

[59] W. Köster, A. Wiskemann, Phototherapy with UV-B in vitiligo, Z. Hautkr. 65 (1990) 1022–1024.

[60] P.D. Belsare, S.V. Moharil, C.P. Joshi, S.K. Omanwar, Preparation and characterization of UV emitting fluoride phosphors for phototherapy lamps, AIP Conf. Proc. 1391 (2011) 194–196.
[61] A.B. Gawande, R.P. Sonekar, S.K. Omanwar, Combustion synthesis of narrow-band UVB emitting borate phosphors LaB_3O_6:Bi, Gd and $YBaB_9O_{16}$:Bi,Gd for phototherapy applications, Optik 127 (2016) 3925–3927.
[62] A.B. Gawande, R.P. Sonekar, S.K. Omanwar, Luminescence improvement in Pr^{3+} and Gd^{3+} activated $Sr_2Mg(BO_3)_2$, inorganic phosphor, Mater. Res. Bull. 60 (2014) 285–291.
[63] V.V. Shinde, R.G. Kunghatkar, S.J. Dhoble, UVB-emitting Gd^{3+}-activated M_2O_2S (where M=La, Y) for phototherapy lamp phosphors, J. Lumin. 30 (2015) 1257–1262.
[64] V. Singh, G. Sivaramaiah, J.L. Rao, S.H. Kim, Luminescence and EPR studies of Gd^{3+}-activated strong UV-emitting $CaZrO_3$ phosphors prepared via solution combustion method, J. Electron. Mater. 43 (2014) 3486–3492.
[65] V. Singh, S. Borkotoky, A. Murali, J.L. Rao, T.K. Gundu Rao, S.J. Dhoble, Electron paramagnetic resonance and photoluminescence investigation on ultraviolet-emitting gadolinium-ion-doped $CaAl_{12}O_{19}$ phosphors, Spectrochm. Acta A 139 (2015) 1–6.
[66] Xiaohua Liu, Xiaodong Wang, Preparation and luminescence properties of $BaZrO_3$: Eu phosphor powders, Opt. Mater. 30 (4) (2007) 626–629.
[67] S.H. Butt, M.S. Rafique, S. Bashir, U. Ilyas, K. Siraj, M.S. Awan, K. Mehmood, M. Rafique, A. Afzal, Influence of Er doping on the structural, optical and luminescence properties of pulsed laser deposited Er: $BaZrO_3$ thin films, Ceram. Int. 43 (15) (2017) 12162–12166.
[68] H. Li, Y. Zhang, L. Shao, Z.M. Htwe, P. Yuan, Ratiometric temperature sensing based on non-thermal coupling levels in $BaZrO_3$:Yb^{3+}/Er^{3+} ceramics, Opt. Mater. Exp. 7 (2017) 3003–3010.
[69] A.I. Lebedev, I.A. Sluchinskaya, Structural instability in $BaZrO_3$ crystals: calculations and experiment, Phys. Solid State 55 (2013) 1941–1945.
[70] J.A. Jiménez, Enhanced UV emission of Gd^{3+} in glass by Ag^{+} co-doping, Mater. Lett. 159 (2015) 193–196.
[71] C. Zuo, A. Lu, L. Zhu, Z. Zhou, W. Long, Luminescent properties of Tb^{3+} and Gd^{3+} ions doped aluminosilicate oxyfluoride glasses, Spectrochm. Acta A 82 (2011) 406–409.
[72] L.H. Brixner, G. Blasse, Gd^{3+} emission from the two crystallographic sites of C-type Y_2O_3, J. Electrochm. Soc. 136 (1989) 3529–3531.
[73] Y. Shimizu, K. Ueda, H. Takashima, Y. Inaguma, UV cathodoluminescence of Gd^{3+} doped and Gd^{3+}, Pr^{3+} co-doped $YAlO_3$ epitaxial thin films, Physica Status Solidi A 212 (2015) 703–706.
[74] H. Dahiya, M. Dalal, J. Dalal, V.B. Taxak, S.P. Khatkar, D. Kumar, Synthesis and luminescent properties of Tb^{3+} doped $BaLa_2ZnO_5$ nanoparticles, Mater. Res. Bull. 99 (2018) 86–92.
[75] S. Parida, S.K. Rout, L.S. Cavalcante, E. Sinha, M.S. Li, V. Subramanian, N. Gupta, V.R. Gupta, J.A. Varela, E. Longo, Structural refinement, optical and microwave dielectric properties of $BaZrO_3$, Ceram. Int. 38 (2012) 2129–2138.
[76] H.D. Megaw, Crystal structure of double oxides of the perovskite type, Proc. Phys. Soc. 58 (1946) 133–152.
[77] D. Truong, M.K. Devaraju, T. Tomai, I. Honma, Direct observation of antisite defects in $LiCoPO_4$ cathode materials by annular dark- and bright-field electron microscopy, ACS Appl. Mater. Interfaces. 5 (2013) 9926–9932.
[78] R.C. Weast, (Ed.), Handbook of Chemistry and Physics, CRC, Cleveland, 1971.
[79] N. Yuan, X. Liu, F. Meng, D. Zhou, First-principles study of La_2CoMnO_6: a promising cathode material for intermediate-temperature solid oxide fuel cells due to intrinsic Co-Mn cation disorder, J. Meng Ionics 21 (2015) 1675–1681.
[80] Y.V. Zorenko, A.S. Voloshinovski, I.V. Konstankevych, Luminescence of F^{+} and F centers in $YAlO_3$, Opt. Spectrosc. 96 (2004) 532–537.
[81] C. Gionco, M.C. Paganini, E. Giamello, R. Burgess, C. Di Valentin, G. Pacchioni, Paramagnetic defects in polycrystalline zirconia:an EPR and DFT study, Chem. Mater. 25 (2013) 2243–2253.
[82] R. Cases, D.L. Griscom, D.C. Tran, Radiation effects in ZrF_4 based glasses: I. Electron spin resonance, J. Non-Cryst. Solids 72 (1985) 51–63.
[83] M.M. Abraham, L.A. Boatner, J.O. Ramey, M. Rappaz, The occurrence and stability of trivalent zirconium in orthophosphate single crystals, J. Chem. Phys. 81 (1984) 5362–5366.
[84] G.R. Asatryan, A.S. Kuzanyan, A.G. Petrosyan, A.K. Petrosyan, E.G. Sharoyan, Optical and EPR absorption spectra of yttrium aluminium garnet single crystals doped by Zr ions, Fizika Tverdogo Tela 27 (1985) 3441–3443.
[85] C.M. Brodbeck, L.E. Iton, The EPR spectra of Gd^{3+} and Eu^{2+} in glassy systems, J. Chem. Phys. 83 (1985) 4285–4299.
[86] R.D. Shannon, Revised effective ionic radii and systematic studies of interatomic distances in halides and chalcogenides, Acta Cryst. A 32 (1976) 751–767.
[87] Y. Hinatsu, Electron paramagnetic resonance spectra of Pr^{4+} in $BaCeO_3$, $BaZrO_3$, $BaSnO_3$, and their solid solutions, J. Solid State Chem. 122 (1996) 384–389.
[88] B.G. Wybourne, Energy levels of trivalent gadolinium and ionic contributions to the ground-state splitting, Phys. Rev. 148 (1966) 317–327.